

Gluon-gluon contributions to W^+W^- production and Higgs interference effects

John M. Campbell, R. Keith Ellis and Ciaran Williams

Fermilab, Batavia, IL 60510, USA

E-mails: johnmc@fnal.gov, ellis@fnal.gov, ciaran@fnal.gov.

ABSTRACT: In this paper we complete our re-assessment of the production of W boson pairs at the LHC, by calculating analytic results for the $gg \rightarrow W^+W^- \rightarrow \nu l^+ l^- \bar{\nu}$ process including the effect of massive quarks circulating in the loop. Together with the one-loop amplitudes containing the first two generations of massless quarks propagating in the loop, these diagrams can give a significant contribution with a large flux of gluons. One of the component parts of this calculation is the production of a standard model Higgs boson, $gg \rightarrow H$ and its subsequent decay, $H \rightarrow W^+(\rightarrow \nu l^+)W^-(\rightarrow l^- \bar{\nu})$. We will quantify the importance of the interference between the Higgs boson production process and the gluon-induced continuum production in the context of searches for the Higgs boson at the Tevatron and the LHC. For instance, for $m_H < 140$ GeV the effect of the interference typically results in around a 10% reduction in the expected number of Higgs signal events. The majority of this interference is due to non-resonant contributions. Therefore cuts on the transverse mass such as those currently used by the ATLAS collaboration reduce the destructive interference to about a 1% effect. We advocate that a cut on the maximum transverse mass be used in future Higgs searches in this channel.

KEYWORDS: QCD, Hadron colliders, LHC.

Contents

1. Introduction	1
2. Calculation	3
2.1 Amplitudes for $gg \rightarrow WW$	3
2.2 Integral basis	4
2.3 Rational part	6
2.4 Bubble coefficients	6
2.5 Box coefficients	7
2.6 Triangle coefficients	8
2.7 Calculation of the Higgs mediated diagrams	10
3. Effect of massive loops in $gg \rightarrow WW$	11
3.1 Parameters	11
3.2 Results	11
4. Higgs $\rightarrow WW$ interference effects at the LHC	14
4.1 No final state cuts	15
4.2 Interference with search cuts	19
5. Higgs $\rightarrow WW$ interference effects at the Tevatron	23
6. Combining the interference with NNLO predictions	25
7. Conclusions	25

1. Introduction

The search for the Standard Model (SM) Higgs boson is entering the closing stages. With the LHC acquiring data at an impressive rate, evidence for the existence of the Higgs boson or its exclusion over the mass range 115 – 600 GeV should be expected by the end of 2012. In addition, ongoing studies at the Tevatron with around 10 fb^{-1} will provide additional independent exclusion regions over a wide range of potential Higgs masses. In summary, the combined results from both hadron colliders can be expected to tightly constrain the Higgs boson within the course of the coming year. Winter 2010 results from the various collaborations can be found in refs. [1–3].

An important Higgs search channel over the range 120 – 200 GeV is the process $gg \rightarrow H \rightarrow WW \rightarrow \nu\ell\ell'\nu'$. This proceeds through gluon fusion via a top (or bottom) loop with the subsequent production of two W bosons that then decay leptonically. In

setting a limit on this channel one needs to possess precise predictions for the cross section and kinematic distributions. Thankfully, as a result of much theoretical work the (fully differential) production cross section for a Higgs boson through gluon fusion is known at NNLO (see for example refs. [4–10]). By including the NNLO corrections one typically finds scale uncertainties on inclusive quantities (which are used to quantify theoretical uncertainty by the collaborations) of $\mathcal{O}(10-20\%)$ [11]. Quoting an error of this order requires that all contributions to the cross section that could possibly change it by $\mathcal{O}(10\%)$ have been calculated, and included in the theoretical predictions used. To correctly exclude the Higgs then, one must confirm that no remaining $\mathcal{O}(10\%)$ effects are neglected in the theoretical prediction.

One potentially large contribution to the cross section is the interference between the Higgs signal and SM continuum production of WW pairs. Power counting in α_S indicates that this contribution is the same order as the LO Higgs signal cross section. Typically these interference terms are neglected in the theoretical calculations used by the collaborations. The aim of this paper is to fully quantify this interference under a variety of experimental cuts. In order to do this we calculate analytic results for the $gg \rightarrow WW \rightarrow \nu l^+ l^- \bar{\nu}$ process including the effect of massive quarks circulating in the loop. The interference has been studied in ref. [12], in which the focus was on a 14 TeV LHC, and on the effects on the total cross section. In this study we will re-address the issue in the context of current Higgs boson searches. The interference effects associated with Higgs production and decay to ZZ have been studied some time ago [13, 14]. In these papers the primary focus was at SSC operating energies and large Higgs masses. Similar studies have also been performed for the case of a light Higgs boson decaying into di-photons at the LHC [15] and the case of Higgs production at a photon collider with subsequent decay into bottom quark pairs [16].

The process $q\bar{q} \rightarrow WW$ was first calculated in the Born approximation in ref. [17], with strong corrections later computed in refs. [18–21]. Phenomenological NLO results for the Tevatron and the LHC have been presented in refs. [22–24]. The gluon-initiated contribution $gg \rightarrow WW$ was first calculated in refs. [13, 25] and later improved to account for off-shell effects of the vector bosons and their subsequent decays in ref. [26]. The effect of massive quarks circulating in the loop was later assessed in ref. [12]. Combined results, including both the $q\bar{q}$ and gg initiated contributions – for loops of massless quarks only – were recently presented in ref. [24]. In this paper we shall use modern methods to provide a calculation of the massive quark contributions that is equivalent to the calculation in ref. [12] and update the results of ref. [24] accordingly.

The plan of this paper is as follows. In section 2 we shall describe the calculation of the amplitude $gg \rightarrow WW$ where a massive top quark (and, where numerically significant, a massive bottom quark) circulates in the loop. Sections 3, 4 and 5 will present phenomenological results using the implementation of these amplitudes into the parton level Monte Carlo program MCFM. Section 3 will address the size of the corrections to the WW process resulting from the inclusion of massive quarks. In sections 4 and 5 we shall discuss the interference contributions at the LHC and Tevatron respectively. In particular we will discuss these effects in the region where cuts are applied to enhance the signal to background ratio for the detection of the Standard Model Higgs boson. In section 6 we

discuss the impact of the interference in regards to the NNLO predictions for the total cross section. Finally, in section 7 we draw our conclusions.

2. Calculation

In reference [24] we showed that the calculation of $gg \rightarrow WW$ with massless quarks circulating in the loop can be extracted from Ref. [27]. Specifically, we find that the contribution from a single generation of massless quarks in the loop is given by,

$$\begin{aligned} & \mathcal{A}_6^{1\text{-loop}} \left(1_g^{h_1}, 2_g^{h_2}, 3_{\nu_\ell}^-, 4_\ell^+, 5_{\ell'}^-, 6_{\bar{\nu}_{\ell'}}^+ \right) \\ &= \delta^{a_1 a_2} \left(\frac{g_w^4 g_s^2}{16\pi^2} \right) \mathcal{P}_W(s_{34}) \mathcal{P}_W(s_{56}) \left[-\frac{1}{c_\Gamma} A_{6;4}^v \left(4_q^+, 3_{\bar{q}}^-, 1_g^{h_1}, 2_g^{h_2}; 5_{\bar{e}}^-, 6_e^+ \right) \right] . \end{aligned} \quad (2.1)$$

The helicities and colour labels of the two gluons are h_1, h_2 and a_1, a_2 respectively and the propagator factor is,

$$\mathcal{P}_W(s) = \frac{s}{s - m_W^2 + i \Gamma_W m_W} , \quad (2.2)$$

where m_W and Γ_W are the mass and width of the W boson. The amplitude $A_{6;4}^v$ and constant c_Γ are defined in Sections 2, 6 and 11 of ref. [27]. The particle labelling on the right hand side of this equation is as written in ref. [27]. For our purposes in Eq. (2.1) we make the identification, ($q \rightarrow \bar{\ell}$, $\bar{q} \rightarrow \nu_\ell$, $\bar{e} \rightarrow \ell'$ and $e \rightarrow \bar{\nu}_{\ell'}$) in going from right to left.

The calculation in Ref. [27] was performed using unitarity methods. Our aim in this section is to perform a similar calculation but including the mass of the top quark circulating in the loop and also the mass of the bottom quark where numerically significant.

2.1 Amplitudes for $gg \rightarrow WW$

In this section we present results for the amplitudes relevant for the process,

$$0 \rightarrow g(p_1) + g(p_2) + \nu_\ell(p_3) + \bar{\ell}(p_4) + \ell'(p_5) + \bar{\nu}_{\ell'}(p_6) . \quad (2.3)$$

Topologies of diagrams that could potentially contribute to the leptonic final state in which we are interested are shown in Fig. 1. When the vector boson couples to the triangular fermion loop (diagrams (a) and (b)) via a vector coupling, the contribution vanishes via Furry's theorem. When the vector boson couples via an axial coupling to massless quarks, the contribution of up-type quarks with weak isospin 1/2 and down-type quarks with weak isospin -1/2 cancel. In the case of the third generation with a massive top quark this cancellation is no longer operative, but it turns out that there is no net contribution [12] as we shall now illustrate. If the masses of the appropriate lepton pairs are constrained to have the mass of the W , the contribution of diagram (a) vanishes and diagram (b) is not present. This follows because the only non-vanishing contribution of the triangle diagram is proportional to p_Z^μ where p_Z is the momentum of the Z boson and μ is its Lorentz index [28]. If this condition is relaxed to allow off-shell W -bosons, the contribution of an individual fermion flavour cancels between the doubly resonant diagrams (a) and the singly resonant diagrams (b). Therefore in both cases the triangle diagrams vanish because of

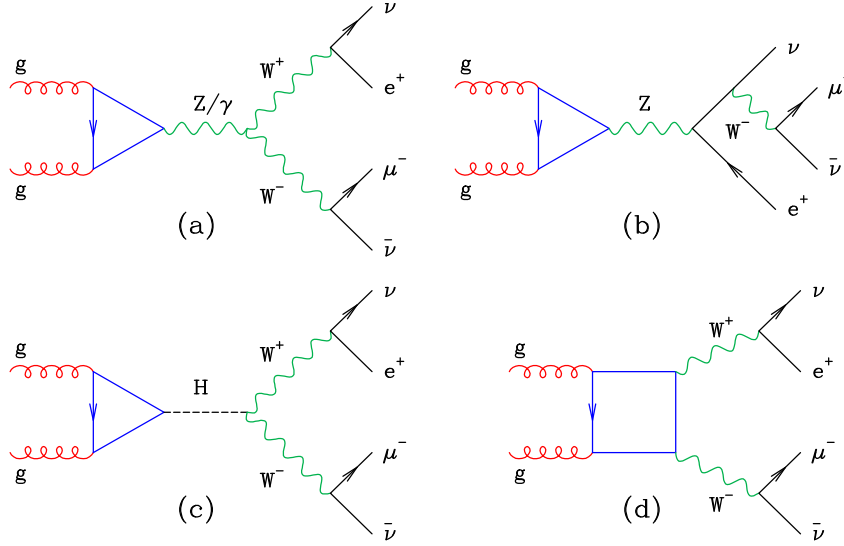


Figure 1: Topologies of diagrams that could potentially contribute the process $gg \rightarrow \nu_e e^+ \mu^- \bar{\nu}_\mu$.

electroweak gauge invariance. Thus the only triangle loop contribution comes from the Higgs boson mediated diagram (c).

We shall therefore separate the calculation of the full amplitude as follows,

$$\mathcal{A}_{\text{full}} = \delta^{a_1 a_2} \left(\frac{g_w^4 g_s^2}{16\pi^2} \right) \mathcal{P}_W(s_{34}) \mathcal{P}_W(s_{56}) [2\mathcal{A}_{\text{massless}} + \mathcal{A}_{\text{massive}} + \mathcal{A}_{\text{Higgs}}] , \quad (2.4)$$

where the first two terms in the square brackets represent the six continuum diagrams shown in Fig. 2. We explicitly separate out the contribution from the first two generations, ($2\mathcal{A}_{\text{massless}}$), in which we consider the quarks in the loop to be massless, and the contribution from the third generation in which the top quark mass is not neglected, $\mathcal{A}_{\text{massive}}$. We have also extracted an overall color, coupling and propagator factor that is the same as in the massless case, so that comparing with Eq. (2.1) we immediately see that,

$$\mathcal{A}_{\text{massless}} = -\frac{1}{c_\Gamma} A_{6;4}^v . \quad (2.5)$$

The final contribution $\mathcal{A}_{\text{Higgs}}$ originates from two triangle diagrams of the type shown in Fig. 1(c).

2.2 Integral basis

We consider the one-loop amplitude $\mathcal{A}_{\text{massive}}$, corresponding to third generation quarks circulating in the loop. In our calculation we retain the dependence on the mass of the top quark but treat the b -quark as massless since the effect of a non-zero value for m_b is at the level of 0.1% [12].

The amplitude can be expanded in terms of scalar integrals and a rational part as follows,

$$\mathcal{A}_{\text{massive}} = \sum_{i=1}^6 d_i D^{(i)} + \sum_{i=1}^{12} c_i C^{(i)} + \sum_{i=1}^6 b_i B^{(i)} + \mathcal{R} . \quad (2.6)$$

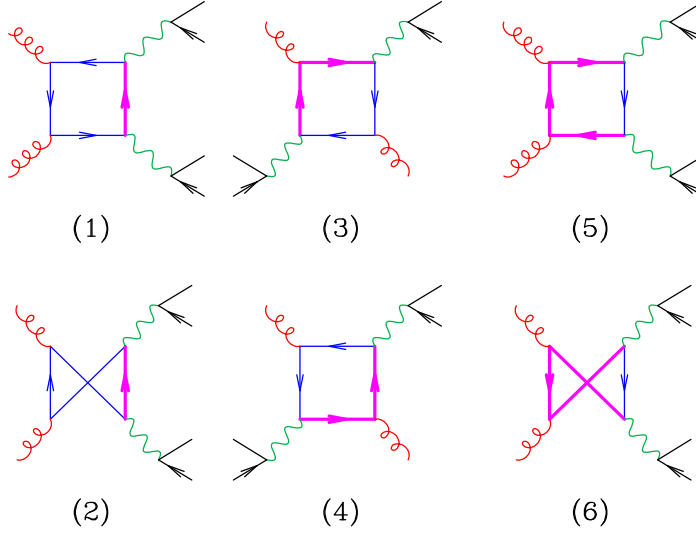


Figure 2: Diagrams that contribute to $gg \rightarrow WW$ with the third generation of quarks running in the loop. The top quark is denoted by a heavy (magenta) line whereas the b bottom quark is shown in blue. The same diagram topologies contribute to the case where first and second generation quarks run in the loop.

$D^{(1)}$	$I_4(s_{34}, 0, 0, s_{56}; s_{134}, s_{12}; m^2, 0, 0, 0)$	$C^{(1)}$	$I_3(0, 0, s_{12}; 0, 0, 0)$
$D^{(2)}$	$I_4(s_{56}, 0, 0, s_{34}; s_{156}, s_{12}; m^2, 0, 0, 0)$	$C^{(2)}$	$I_3(0, s_{134}, s_{34}; 0, 0, m^2)$
$D^{(3)}$	$I_4(s_{56}, 0, s_{34}, 0; s_{156}, s_{134}; 0, m^2, m^2, 0)$	$C^{(3)}$	$I_3(0, s_{56}, s_{134}; 0, 0, m^2)$
$D^{(4)}$	$I_4(s_{56}, 0, s_{34}, 0; s_{156}, s_{134}; m^2, 0, 0, m^2)$	$C^{(4)}$	$I_3(0, s_{156}, s_{56}; 0, 0, m^2)$
$D^{(5)}$	$I_4(s_{34}, 0, 0, s_{56}; s_{134}, s_{12}; 0, m^2, m^2, m^2)$	$C^{(5)}$	$I_3(0, s_{34}, s_{156}; 0, 0, m^2)$
$D^{(6)}$	$I_4(s_{56}, 0, 0, s_{34}; s_{156}, s_{12}; 0, m^2, m^2, m^2)$	$C^{(6)}$	$I_3(s_{12}, s_{56}, s_{34}; 0, 0, m^2)$
$B^{(1)}$	$I_2(s_{12}; 0, 0)$	$C^{(7)}$	$I_3(s_{134}, 0, s_{34}; 0, m^2, m^2)$
$B^{(2)}$	$I_2(s_{34}; 0, m^2)$	$C^{(8)}$	$I_3(s_{56}, 0, s_{134}; 0, m^2, m^2)$
$B^{(3)}$	$I_2(s_{56}; 0, m^2)$	$C^{(9)}$	$I_3(s_{156}, 0, s_{56}; 0, m^2, m^2)$
$B^{(4)}$	$I_2(s_{134}; 0, m^2)$	$C^{(10)}$	$I_3(s_{34}, 0, s_{156}; 0, m^2, m^2)$
$B^{(5)}$	$I_2(s_{156}; 0, m^2)$	$C^{(11)}$	$I_3(s_{56}, s_{12}, s_{34}; 0, m^2, m^2)$
$B^{(6)}$	$I_2(s_{12}; m^2, m^2)$	$C^{(12)}$	$I_3(s_{12}, 0, 0; m^2, m^2, m^2)$

Table 1: Definitions of the scalar integrals that appear in the calculation of the amplitude $\mathcal{A}_{\text{massive}}$, i.e. continuum production of $gg \rightarrow W^+W^-$ through a loop containing at least one massive particle.

The scalar integrals $B^{(i)}$, $C^{(i)}$, $D^{(i)}$ that contribute to this particular amplitude are listed in Table 1. The coefficients b_i , c_i , d_i are amenable to calculation by unitarity cuts; the contribution \mathcal{R} represents the remaining non-cut-constructible rational part. We have performed a complete independent numerical check of our analytic calculation of the coefficients and the rational part using D -dimensional unitarity [29]. No tadpole contributions are found to be present.

The D -dimensional scalar integrals themselves are defined as follows,

$$\begin{aligned}
I_2(p_1^2; m_1^2, m_2^2) &= \frac{\mu^{4-D}}{i\pi^{\frac{D}{2}} r_\Gamma} \int d^D l \frac{1}{(l^2 - m_1^2 + i\varepsilon)((l + q_1)^2 - m_2^2 + i\varepsilon)}, \\
I_3(p_1^2, p_2^2, p_3^2; m_1^2, m_2^2, m_3^2) &= \frac{\mu^{4-D}}{i\pi^{\frac{D}{2}} r_\Gamma} \\
&\times \int d^D l \frac{1}{(l^2 - m_1^2 + i\varepsilon)((l + q_1)^2 - m_2^2 + i\varepsilon)((l + q_2)^2 - m_3^2 + i\varepsilon)}, \\
I_4(p_1^2, p_2^2, p_3^2, p_4^2; s_{12}, s_{23}; m_1^2, m_2^2, m_3^2, m_4^2) &= \frac{\mu^{4-D}}{i\pi^{\frac{D}{2}} r_\Gamma} \\
&\times \int d^D l \frac{1}{(l^2 - m_1^2 + i\varepsilon)((l + q_1)^2 - m_2^2 + i\varepsilon)((l + q_2)^2 - m_3^2 + i\varepsilon)((l + q_3)^2 - m_4^2 + i\varepsilon)},
\end{aligned} \tag{2.7}$$

where $q_n \equiv \sum_{i=1}^n p_i$ and $s_{ij} = (p_i + p_j)^2$. For the purposes of this paper we take the masses in the propagators to be real. Near four dimensions we use $D = 4 - 2\epsilon$ (and for clarity the small imaginary part which fixes the analytic continuations is specified by $+i\varepsilon$). μ is a scale introduced so that the integrals preserve their natural dimensions, despite excursions away from $D = 4$. We have removed the overall constant which occurs in D -dimensional integrals

$$r_\Gamma \equiv \frac{\Gamma^2(1 - \epsilon)\Gamma(1 + \epsilon)}{\Gamma(1 - 2\epsilon)} = \frac{1}{\Gamma(1 - \epsilon)} + \mathcal{O}(\epsilon^3) = 1 - \epsilon\gamma + \epsilon^2 \left[\frac{\gamma^2}{2} - \frac{\pi^2}{12} \right] + \mathcal{O}(\epsilon^3). \tag{2.8}$$

The final numerical evaluation of the amplitudes uses the QCDLoop library [30] to provide values for these scalar integrals.

2.3 Rational part

In calculating the box diagrams we shall start with the least challenging terms in Fig. 2 using the decomposition of Eq. (2.6). The rational terms are completely determined by the massless calculation which has been already presented. The box diagrams are of rank four, i.e. they contain at most four powers of the loop momentum in the numerator. However the first mass dependent terms contain at least two powers of the mass from numerator factors and are therefore at most of rank two. These contributions are cut-constructible [27] and do not contribute to the rational part. The rational terms are controlled by the ultraviolet behavior and thus the presence of masses in the denominators of the rank 3 and 4 boxes does not change the rational part. The rational part is therefore identical to the massless case. This assertion has been checked by direct numerical evaluation.

2.4 Bubble coefficients

Turning now to the coefficients of the bubble integrals, we find numerically that the results for the massless case can be re-used for the massive case. In the limit that the internal mass m vanishes, we see that the integrals $B^{(1)}$ and $B^{(6)}$ become degenerate. Therefore the integral $B^{(6)}$ can be dropped from the basis and we can write the bubble contributions

to the amplitude for the massless calculation as a sum over only 5 terms,

$$\sum_{i=1,5} b_{\text{massless}}^{(i)} B_{\text{massless}}^{(i)} . \quad (2.9)$$

In this equation the subscript “massless” labels the coefficient in the massless calculation and $B_{\text{massless}}^{(i)} = B^{(i)}|_{m=0}$. We find that four of the integral coefficients are identical to the massless case,

$$b^{(i)} = b_{\text{massless}}^{(i)} \quad \text{for } i = 2, 3, 4, 5 . \quad (2.10)$$

Moreover, the sum of the two remaining coefficients is equal to the final massless coefficient,

$$b^{(1)} + b^{(6)} = b_{\text{massless}}^{(1)} , \quad (2.11)$$

as a result of the fact that the amplitude does not contain any poles of ultraviolet origin,

$$\sum_{i=1,6} b^{(i)} = 0 . \quad (2.12)$$

We have performed an explicit calculation of the simplest coefficient ($b^{(1)}$) (using the technique described in [31]) and have hence determined all six of the bubble coefficients from the known massless bubble coefficients in Ref. [27].

2.5 Box coefficients

We express the amplitudes in terms of spinor products defined as,

$$\langle i j \rangle = \bar{u}_-(p_i) u_+(p_j), \quad [i j] = \bar{u}_+(p_i) u_-(p_j), \quad \langle i j \rangle [j i] = 2 p_i \cdot p_j , \quad (2.13)$$

and we further define the spinor sandwich,

$$\langle i | (j + k) | l \rangle = \langle i j \rangle [j l] + \langle i k \rangle [k l] . \quad (2.14)$$

In order to express the amplitudes compactly we define two symmetry operations,

$$\text{flip}_1 := \left\{ (3 \leftrightarrow 6), (4 \leftrightarrow 5), \langle \rangle \leftrightarrow [] \right\} , \quad (2.15)$$

$$\text{flip}_2 := \left\{ (1 \leftrightarrow 2), (3 \leftrightarrow 6), (4 \leftrightarrow 5), \langle \rangle \leftrightarrow [] \right\} , \quad (2.16)$$

which we will use to relate various coefficients in the amplitude. Specifically for the box coefficients in Eq. (2.6) related to the box integrals with the labels given in Table 1 we have,

$$d_{2,6}^{++} = \text{flip}_1 d_{1,5}^{--}, \quad d_{2,6}^{--} = \text{flip}_1 d_{1,5}^{++}, \quad d_{2,6}^{+-} = \text{flip}_1 d_{1,5}^{+-}, \quad d_{2,6}^{-+} = \text{flip}_1 d_{1,5}^{-+} . \quad (2.17)$$

Finally the relations between the coefficients for boxes 3 and 4 are,

$$d_4^{++} = \text{flip}_2 d_3^{--}, \quad d_4^{--} = \text{flip}_2 d_3^{++}, \quad d_4^{+-} = \text{flip}_2 d_3^{-+}, \quad d_4^{-+} = \text{flip}_2 d_3^{+-} . \quad (2.18)$$

Note, in particular, that the flip_2 symmetry relates the $(-, +)$ coefficients of boxes 3 and 4 whereas flip_1 relates d_2^{++} to d_1^{--} .

Given these relations, it is therefore sufficient to compute the coefficients d_1, d_3 and d_5 , which we do using the quadruple cut method [32]. The simplest coefficients are those of the boxes containing only a single massive propagator,

$$\begin{aligned}
d_1^{++} &= 0 , \\
d_1^{--} &= 0 , \\
d_1^{+-} &= -\frac{i}{2} \frac{s_{12}}{s_{34}s_{56}} \frac{\langle 13 \rangle [26] (m^2 - s_{134})^3}{\langle 1|(3+4)|2]^4} (\langle 13 \rangle [34] \langle 56 \rangle [26] + m^2 \langle 15 \rangle [42]) \\
d_1^{-+} &= -\frac{i}{2} \frac{s_{12}}{s_{34}s_{56}} \frac{(m^2 - s_{134})}{\langle 2|(3+4)|1]^4} (m^2 [41] \langle 25 \rangle + \langle 2|(1+3)|4] \langle 5|(3+4)|1]) , \\
&\quad (m^2 [16] - [56] \langle 5|(2+6)|1]) (m^2 \langle 23 \rangle + \langle 34 \rangle \langle 2|(1+3)|4]) . \tag{2.19}
\end{aligned}$$

The coefficients of the boxes containing two massive propagators are more complicated but still relatively compact,

$$\begin{aligned}
d_3^{++} &= \frac{i}{2} \frac{1}{s_{34}s_{56}} \frac{(s_{134}s_{156} - s_{56}s_{34} + m^2 s_{12}) \langle 23 \rangle}{s_{12}^2 \langle 12 \rangle^2} \left(\langle 15 \rangle [56] [12] + [16] \frac{m^2 s_{12}}{\langle 2|(5+6)|1]} \right) \\
&\quad \left(\langle 15 \rangle \langle 23 \rangle [34] [12] - \langle 25 \rangle [14] \frac{m^2 s_{12}}{\langle 2|(5+6)|1]} \right) , \\
d_3^{+-} &= \frac{i}{2} \frac{1}{s_{34}s_{56}} \frac{m^2 (s_{134}s_{156} - s_{56}s_{34} + m^2 s_{12}) [26]}{s_{12}^2 \langle 1|(5+6)|2]^2} \left(\langle 12 \rangle \langle 43 \rangle [14] - \langle 13 \rangle \frac{m^2 s_{12}}{\langle 1|(5+6)|2]} \right) \\
&\quad \left(\langle 12 \rangle [14] \langle 5|(3+4)|2] - \langle 15 \rangle [24] \frac{m^2 s_{12}}{\langle 1|(5+6)|2]} \right) , \\
d_3^{--} &= \text{flip}_1 d_3^{++} , \\
d_3^{-+} &= \text{flip}_1 d_3^{+-} . \tag{2.20}
\end{aligned}$$

The coefficients of box 5 are lengthier; interested readers may inspect their form in the distributed MCFM code.

2.6 Triangle coefficients

Turning now to the coefficients of triangle integrals, we see from Table 1 that twelve coefficients are required. These triangle integrals are depicted in Figure 3. Since the amplitude that we are calculating is finite, all of the poles in ϵ must cancel. This cancellation of infrared poles leads to relations between the triangle coefficients and the singular boxes 1–4. In particular we find that c_1, c_2, c_3, c_4 and c_5 can be determined in terms of these box coefficients through the set of equations,

$$\frac{d_1}{s_{134} - m^2} + \frac{d_2}{s_{156} - m^2} + c_1 = 0 , \tag{2.21}$$

$$\frac{d_4}{\Delta} + \frac{d_1}{s_{12}(s_{134} - m^2)} + \frac{c_2}{s_{134} - s_{34}} = 0 , \tag{2.22}$$

$$\frac{d_3}{\Delta} + \frac{d_1}{s_{12}(s_{134} - m^2)} + \frac{c_3}{s_{134} - s_{56}} = 0 , \tag{2.23}$$

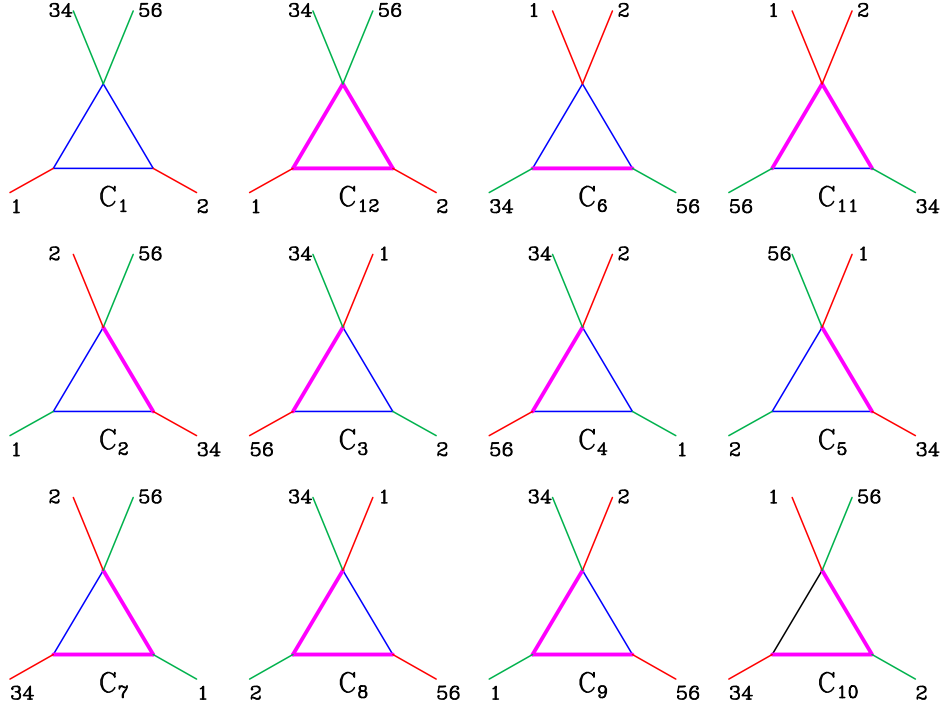


Figure 3: Scalar triangle integrals present in the calculation.

$$\frac{d_4}{\Delta} + \frac{d_2}{s_{12}(s_{156} - m^2)} + \frac{c_4}{s_{156} - s_{56}} = 0 , \quad (2.24)$$

$$\frac{d_3}{\Delta} + \frac{d_2}{s_{12}(s_{156} - m^2)} + \frac{c_5}{s_{156} - s_{34}} = 0 . \quad (2.25)$$

These relations involve a kinematic factor Δ related to boxes 3 and 4, where Δ is given by,

$$\Delta = (m^2 - s_{134})(m^2 - s_{156}) - (m^2 - s_{34})(m^2 - s_{56}) . \quad (2.26)$$

Therefore it only remains to determine c_i for $i = 6-12$. Many of these coefficients are related to one another by the flip operations defined in Eqs. (2.15,2.16) or simpler symmetries. In particular we find that the different helicity amplitudes for triangle 6 are related,

$$\begin{aligned} c_6^{--} &= c_6^{++}(1 \leftrightarrow 2) , \\ c_6^{-+} &= c_6^{+-}(1 \leftrightarrow 2) , \end{aligned} \quad (2.27)$$

whereas the flip_1 symmetry of Eq. (2.15) relates the coefficients of triangles 7 and 9,

$$\begin{aligned} c_9^{--} &= \text{flip}_1 c_7^{++} , \\ c_9^{++} &= \text{flip}_1 c_7^{--} , \\ c_9^{-+} &= \text{flip}_1 c_7^{+-} , \\ c_9^{+-} &= \text{flip}_1 c_7^{-+} . \end{aligned} \quad (2.28)$$

The coefficients c_8 and c_{10} can be determined from those for c_7 and c_9 using the relations,

$$c_{8,10}^{--} = c_{9,7}^{--}(1 \leftrightarrow 2) ,$$

$$\begin{aligned}
c_{8,10}^{++} &= c_{9,7}^{++} (1 \leftrightarrow 2) , \\
c_{8,10}^{-+} &= c_{9,7}^{-+} (1 \leftrightarrow 2) , \\
c_{8,10}^{+-} &= c_{9,7}^{+-} (1 \leftrightarrow 2) .
\end{aligned} \tag{2.29}$$

Finally, we have the relationships between the different helicity amplitudes for triangle 11,

$$\begin{aligned}
c_{11}^{--} &= c_{11}^{++} \left\{ (1 \leftrightarrow 2), (3 \leftrightarrow 4), (5 \leftrightarrow 6), \langle \rangle \leftrightarrow [] \right\} , \\
c_{11}^{-+} &= c_{11}^{+-} (1 \leftrightarrow 2) ,
\end{aligned} \tag{2.30}$$

and triangle 12,

$$\begin{aligned}
c_{12}^{--} &= \text{flip}_1 c_{12}^{++} , \\
c_{12}^{-+} &= \text{flip}_1 c_{12}^{+-} .
\end{aligned} \tag{2.31}$$

We have calculated the coefficients of the remaining unconstrained triangles using the method of [33]. The results for these triangle coefficients are complicated but may be inspected in the distributed MCFM code.

2.7 Calculation of the Higgs mediated diagrams

The calculation of Higgs boson production via a loop of heavy quarks is well known. Here we also include the decay of the Higgs boson into a pair of W bosons, with our usual particle labelling. The contribution to the full amplitude is then,

$$\mathcal{A}_{\text{Higgs}}^{h_1, h_2} = K^{h_1, h_2} \mathcal{P}_H(s_{12}) \sum_{q=t, b} \left[c_H(m_q) I_3(s_{12}, 0, 0; m_q^2, m_q^2, m_q^2) + \mathcal{R}_H(m_q) \right] , \tag{2.32}$$

where overall factors of color, couplings and W propagators have been extracted in Eq. (2.4). Note that here we sum over both top and bottom quark loops since the effect of including the bottom quark contribution is numerically important for lower Higgs masses (through its interference with the top quark loops). Although we have therefore treated the bottom quark mass in an inconsistent manner (finite in the loops coupling to a Higgs boson, zero otherwise), we have checked that the discrepancy is not phenomenologically relevant. Although including the mass of the bottom quark can significantly change the total production rate for a light Higgs, the interference terms that are the focus of this paper have a very small dependence on m_b . The dependence on the helicities of the gluons is encoded in the factor K^{h_1, h_2} which is given by,

$$\begin{aligned}
K^{-+} &= K^{+-} = 0 , \\
K^{--} &= \frac{2 \langle 1 2 \rangle \langle 3 5 \rangle [6 4]}{[2 1] s_{34} s_{56}} , \\
K^{++} &= \frac{2 [1 2] \langle 3 5 \rangle [6 4]}{\langle 2 1 \rangle s_{34} s_{56}} .
\end{aligned} \tag{2.33}$$

The coefficient of the scalar triangle and the rational contribution are,

$$c_H(m) = -\frac{im^2}{2} \left(1 - \frac{4m^2}{s_{12}} \right) , \quad \mathcal{R}_H(m) = \frac{im^2}{s_{12}} . \tag{2.34}$$

Substituting for $I_3(s_{12}, 0, 0; m_q^2, m_q^2, m_q^2)$ in Eq. (2.32) we obtain,

$$\mathcal{A}_{\text{Higgs}}^{h_1, h_2} = \frac{iK^{h_1, h_2} \mathcal{P}_H(s_{12})}{2} \sum_{q=t, b} \frac{m_q^2}{s_{12}} \left[2 + \left(\frac{4m_q^2}{s_{12}} - 1 \right) F \left(\frac{m_q^2}{s_{12}} \right) \right], \quad (2.35)$$

where the function $F(x)$ is defined by,

$$F(x) = \begin{cases} \frac{1}{2} \left[\log \left(\frac{1+\sqrt{1-4x}}{1-\sqrt{1-4x}} \right) - i\pi \right]^2, & x < 1/4, \\ -2 \left[\sin^{-1}(1/2\sqrt{x}) \right]^2, & x \geq 1/4. \end{cases} \quad (2.36)$$

Up to overall factors that are associated with the decay $H \rightarrow WW$, this is the well-known result (see e.g. Ref. [34]).

3. Effect of massive loops in $gg \rightarrow WW$

3.1 Parameters

The results presented in this paper are obtained with the latest version of the MCFM code (v6.1). We use the default set of electroweak parameters that assumes the following set of inputs,

$$\begin{aligned} m_W &= 80.398 \text{ GeV}, \quad m_Z = 91.1876 \text{ GeV}, \\ \Gamma_W &= 2.1054 \text{ GeV}, \quad \Gamma_Z = 2.4952 \text{ GeV}, \\ G_F &= 1.16639 \times 10^{-5} \text{ GeV}^{-2}. \end{aligned} \quad (3.1)$$

Using the values of m_W , m_Z and G_F as above then determines $\alpha_{e.m.}(m_Z)$ and $\sin^2 \theta_w$ as outputs, where θ_w is the Weinberg angle. We find,

$$\begin{aligned} \sin^2 \theta_w &= 1 - m_W^2/m_Z^2 = 0.222646, \\ \alpha_{e.m.}(m_Z) &= \frac{\sqrt{2}G_F m_W^2 \sin^2 \theta_w}{\pi} = \frac{1}{132.338}. \end{aligned} \quad (3.2)$$

Where massive loops of top and bottom quarks are included we use $m_t = 172.5 \text{ GeV}$ and $m_b = 4.4 \text{ GeV}$. When we include the contribution from diagrams involving a Higgs boson, the values of the width that we use are taken from HDECAY [35] and are shown in Table 2.

For the parton distribution functions (pdfs) we use the sets of Martin, Stirling, Thorne and Watt [36]. We use the NLO pdf fit, with $\alpha_s(m_Z) = 0.12018$ and 2-loop running. In this section we will use a common renormalization and factorization scale equal to m_W . In the following sections, where the interference with the Higgs amplitudes is studied, the common scale (unless otherwise stated) will be set equal to m_H .

3.2 Results

We begin by assessing the numerical impact of the contribution arising from the loops containing massive quarks, i.e. the (t, b) doublet represented by the term $\mathcal{A}_{\text{massive}}$ in Eq. (2.4). This contribution was neglected in the analysis of ref. [24] based on earlier studies at the 14 TeV LHC where it was found to be very small [12].

m_H [GeV]	Γ_H [GeV]	m_H [GeV]	Γ_H [GeV]
100	0.2573×10^{-2}	220	2.301
110	0.2938×10^{-2}	240	3.397
120	0.3600×10^{-2}	260	4.767
130	0.5006×10^{-2}	280	6.443
140	0.8281×10^{-2}	300	8.452
150	0.1744×10^{-1}	320	10.81
155	0.3042×10^{-1}	340	13.50
160	0.8255×10^{-1}	360	17.57
165	0.2434	380	23.04
170	0.3760	400	29.16
180	0.6291	450	46.82
190	1.036	500	67.94
200	1.426	600	122.5

Table 2: Total Higgs width as a function of the Higgs mass using the HDECAY code (v3.51) from ref. [35].

For now we neglect the contribution $\mathcal{A}_{\text{Higgs}}$ in Eq. (2.4) and consider only the effect arising from adding the amplitude $\mathcal{A}_{\text{massive}}$ to the result for two massless doublets of quarks only. We note that adding the massive doublet results in new contributions from both $\mathcal{A}_{\text{massive}}$ and the interference term, $2\text{Re}(\mathcal{A}_{\text{massive}}\mathcal{A}_{\text{massless}}^*)$. In the results that we present here we will compare three contributions to the WW final state:

$\sigma_{gg}[n_{\text{gen}} = 2]$: the gluon-initiated contribution for two massless doublets resulting from the term $2\mathcal{A}_{\text{massless}}$ in Eq. (2.4);

$\sigma_{gg}[n_{\text{gen}} = 3]$: the gluon-initiated contribution for all three doublets resulting from the combination $2\mathcal{A}_{\text{massless}} + \mathcal{A}_{\text{massive}}$ in Eq. (2.4);

$\sigma_{\text{tot}}^{\text{NLO}}$: the total prediction obtained by adding $\sigma_{gg}[n_{\text{gen}} = 3]$ and the NLO result ($q\bar{q}$, gq , $g\bar{q}$ initial states) [22, 24].

Our results for these cross sections, for the production of the final state $W^+(\rightarrow \nu_e e^+)W^-(\rightarrow \mu^- \bar{\nu}_\mu)$, are shown in Table 3. We consider various values of the hadronic collider energy \sqrt{s} , with proton-antiproton collisions at $\sqrt{s} = 1.96$ TeV and proton-proton collisions otherwise. In these calculations we have applied no cuts to the final state.

We first observe that including the third generation has only a minor effect on the gluon-gluon initiated contribution, ranging from an increase of 6% at the Tevatron to an increase of 13% at the 14 TeV LHC. This small increase is washed out even further when considering the correction to the total cross section including $q\bar{q}$, gq and $g\bar{q}$ contributions. As expected, the gluon-gluon contribution is negligible at the Tevatron (0.4% of the total)

\sqrt{s} [TeV]	1.96 ($p\bar{p}$)	7	8	10	12	14
$\sigma_{gg}[n_{\text{gen}} = 2]$	0.460(0)	13.74(1)	18.19(1)	28.37(2)	40.06(3)	52.99(4)
$\sigma_{gg}[n_{\text{gen}} = 3]$	0.490(1)	15.16(1)	20.12(2)	31.61(3)	44.84(4)	59.59(4)
$\sigma_{gg}[n_{\text{gen}} = 3]/\sigma_{gg}[n_{\text{gen}} = 2]$	1.065	1.103	1.106	1.114	1.119	1.125
$\sigma_{\text{tot}}^{NLO}$	134.6(2)	539(1)	657(1)	904(1)	1162(1)	1429(2)
$\sigma_{gg}[n_{\text{gen}} = 3]/\sigma_{\text{tot}}^{NLO}$	0.0036	0.028	0.030	0.035	0.039	0.042

Table 3: Cross sections for the process $W^+(\rightarrow \nu_e e^+)W^-(\rightarrow \mu^- \bar{\nu}_\mu)$ (in femtobarns) with no cuts applied. The cross section resulting from the gluon-gluon initial state (σ_{gg}) is broken down by the number of generations of quarks circulating in the loop. The result with three generations is also compared with the total cross section ($\sigma_{\text{tot}}^{NLO}$), obtained by also including the NLO corrections to the quark-antiquark initial state.

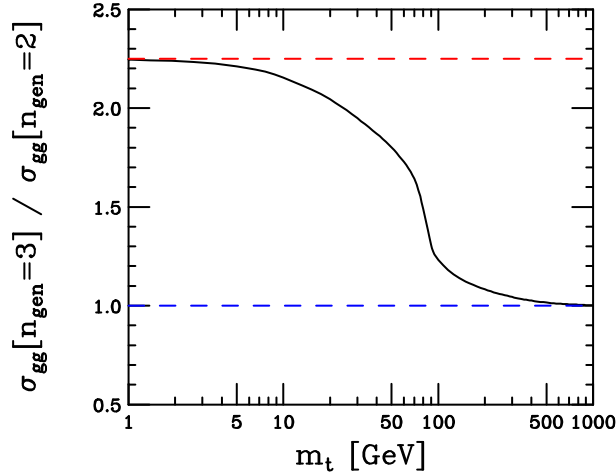


Figure 4: The ratio of $\sigma_{gg}[n_{\text{gen}} = 3]$ to $\sigma_{gg}[n_{\text{gen}} = 2]$ as a function of the top quark mass m_t . The expected results for two and three massless generations are shown as dashed blue (lower) and red (upper) lines respectively.

and even at the LHC it is at most 4% of the total at the highest energy foreseen (although this can increase upon application of various cuts on the final state [12, 24]). We note that our findings at 14 TeV are in complete agreement with the results presented in Ref. [12].

The fact that the three-generation cross section is so close to the two-generation result may be somewhat unexpected. For that reason, in Fig. 4 we illustrate the dependence of $\sigma_{gg}[n_{\text{gen}} = 3]$ on the top quark mass, m_t . In the limit of a very light top quark the third generation is equivalent to the two massless generations, and as a result $\sigma_{gg}[n_{\text{gen}} = 3] \rightarrow \sigma_{gg}[n_{\text{gen}} = 2] \times 9/4$ as $m_t \rightarrow 0$. In the opposite limit, when the top quark is very heavy, the third generation decouples so that $\sigma_{gg}[n_{\text{gen}} = 3] \rightarrow \sigma_{gg}[n_{\text{gen}} = 2]$ as $m_t \rightarrow \infty$. The behaviour of the three-generation result changes rapidly in the region $m_t \sim m_W$, as could be expected from the kinematics of the final state.

In Fig. 5 we present the p_T distribution of one of the W bosons for the first two generations (red) and third generation only (blue). We observe that at low p_T the contribution

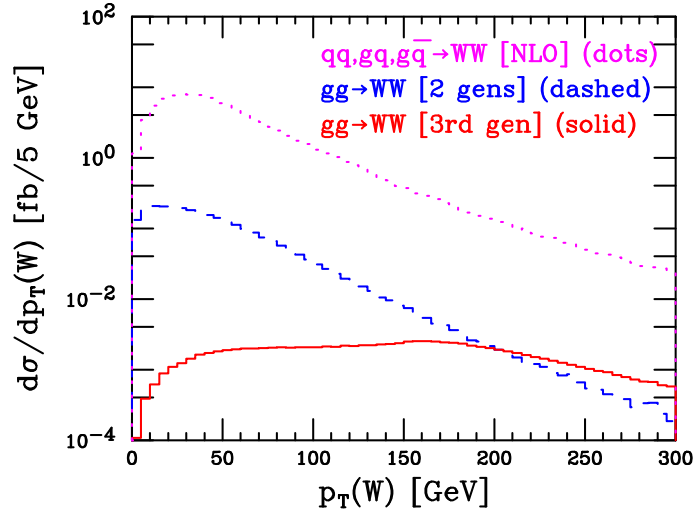


Figure 5: The transverse momentum distribution of the W bosons at $\sqrt{s} = 7$ TeV and with no cuts applied. The contribution from $gg \rightarrow WW$ through a loop of third generation quarks only is shown in solid red and the contribution from $gg \rightarrow WW$ through two massless generations is shown in dashed blue. The distribution obtained from the NLO calculation of the $q\bar{q}, gq, g\bar{q}$ processes is shown as the dotted magenta curve.

from the third generation is negligible but in the region $p_T > m_t$ it becomes increasingly more important. This indicates that for searches that require a high- p_T W boson, the top loops should not be neglected. Numerical instabilities exist in the massive (and to a lesser extent in the massless) calculation in the region of low p_T^W . The origin of these instabilities can be traced back to terms of the form $1/\langle 2|3+4|1 \rangle^n$ in the n -point integral coefficients, for instance in Eq. (2.19) (for $n = 4$). Such denominators clearly vanish in the limit that the momentum $(3+4)$ is collinear to either particle 1 or 2, i.e. the momentum $p_W = p_3 + p_4$ is along the beam, so that $p_T(W) = 0$. The amplitude may be re-expressed in terms of combinations of the scalar integrals that are finite in this limit, a refinement that has already been partially performed for the massless amplitudes [27]. We find that some numerical instability still remains for the massless amplitudes and, in the massive case, the denominators are both more prevalent and more cumbersome to remove. Therefore to ensure numerical stability we instead simply impose a cut, $p_T^W > 2$ (0.05) GeV in the massive (massless) calculation. The application of this cut changes the total cross section by at most 0.05%.

4. Higgs $\rightarrow WW$ interference effects at the LHC

Since we have seen that the effect of the gluon-gluon initial state is largest at the LHC we shall first present phenomenological results applicable for Higgs boson searches at $\sqrt{s} = 7$ TeV. In particular in this section we will consider interference effects between terms in the amplitude that result from diagrams involving a Higgs boson and those that do not.

cut selection	total cross section			search cuts		
M_H [GeV]	140	170	200	140	170	200
σ_H	79.90	116.2	75.39	1.884	12.95	1.664
$\sigma_{H,i}$	72.49	114.4	74.52	1.758	13.84	1.999
$\sigma_{H,i}$ (extracted from Ref. [12])	72.56	114.6	74.45	1.760	13.87	1.999

Table 4: A comparison of results obtained from our calculation in MCFM with the corresponding values extracted from Table 3 of Binoth et al. [12]. Both W 's decay leptonically into a single lepton flavor, no cuts are applied, $\sqrt{s} = 14$ TeV and cross sections are given in femtobarns. The cross sections are computed either excluding (σ_H) or including ($\sigma_{H,i}$) the effect of interference with the gluon-initiated background process.

The cross sections that we shall compute are obtained from Eq. (2.4) by selecting various terms in the square of the amplitude, integrating over the final-state phase space and convoluting with parton density functions appropriately. We shall divide the full contribution to the cross section as follows,

$$\begin{aligned}
\sigma_B &\longrightarrow |\mathcal{A}_{\text{box}}|^2, & \mathcal{A}_{\text{box}} &= 2\mathcal{A}_{\text{massless}} + \mathcal{A}_{\text{massive}}, \\
\sigma_H &\longrightarrow |\mathcal{A}_{\text{Higgs}}|^2, \\
\sigma_i &\longrightarrow 2\text{Re}(\mathcal{A}_{\text{Higgs}}\mathcal{A}_{\text{box}}^*), \\
\sigma_{H,i} &= \sigma_H + \sigma_i.
\end{aligned} \tag{4.1}$$

For a given Higgs mass the total cross section including the Higgs diagram is thus the sum of the first three terms. σ_B and σ_H are the usual leading order gg background and Higgs signal cross sections respectively. When the interference is included, we consider the quantity $\sigma_{H,i}$ as representing the cross section for events containing a Higgs boson, to be compared with the background-only cross section σ_B . We note that, since $\sigma_{H,i}$ is not a physical cross section and therefore not constrained to be positive, we may (and indeed do) find that $\sigma_{H,i} < \sigma_H$.

To validate our computation of the interference terms we first compare our results with those presented in Ref. [12] for the LHC energy of $\sqrt{s} = 14$ TeV. As already noted, in this reference the dependence on the bottom quark mass is retained but here we have chosen to set it to zero. The expected difference, of the order of 0.1%, is at the same level as the Monte Carlo uncertainty in our result. Within these uncertainties, the two calculations are in complete agreement for a range of Higgs masses and cuts, as can be seen from Table 4. For the purposes of this comparison all parameters in MCFM have been set to the values used in Ref. [12]. Ref. [12] also specifies the Higgs search cuts used in the final three columns of the table. Although the quantity $\sigma_{H,i}$ is not explicitly given in Ref. [12] it may easily be extracted from the results presented there.

4.1 No final state cuts

We now return to the case at hand, namely the LHC operating at 7 TeV. The quantities σ_H and $\sigma_{H,i}$, with no cuts applied on the final state, are shown as function of m_H in Fig. 6.

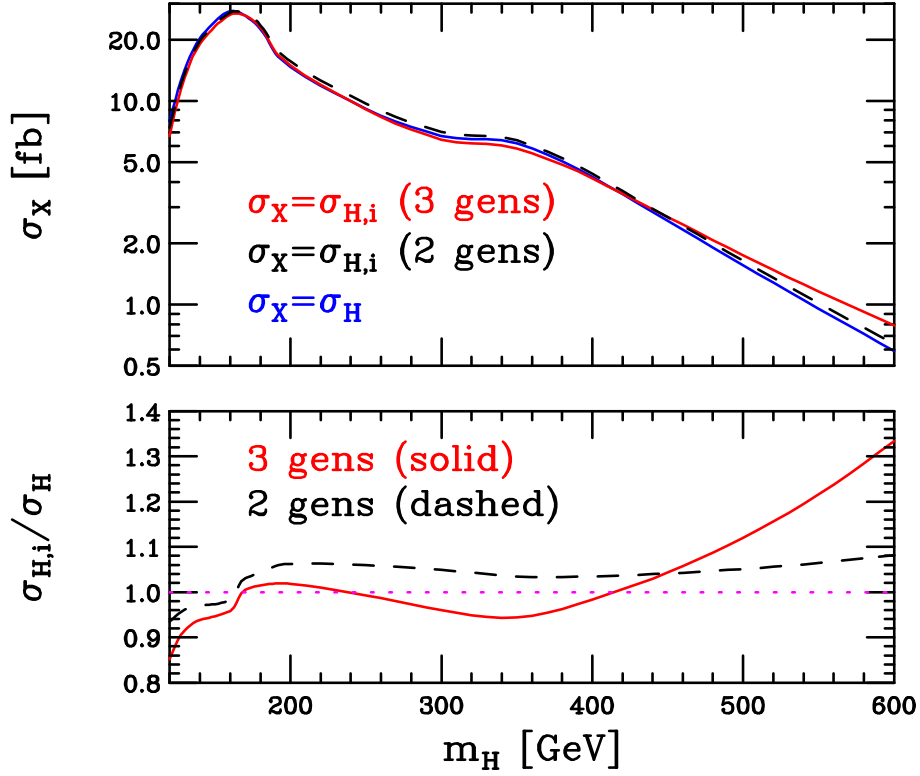


Figure 6: Upper panel: The cross sections for $gg \rightarrow H \rightarrow W^+(\rightarrow \nu_e e^+)W^-(\rightarrow \mu^- \bar{\nu}_\mu)$ in femtobarns, with ($\sigma_{H,i}$) and without (σ_H) the interference with SM $gg \rightarrow WW$ production. The dashed line represents the calculation of $\sigma_{H,i}$ including only the first two generations of quarks. Lower panel: The ratio of the cross sections with and without the interference terms. The dotted magenta line highlights the boundary between constructive and destructive interference.

M_H [GeV]	120	140	170	200	400
σ_H	7.90(1)	20.29(1)	26.13(2)	14.69(1)	4.23(1)
$\sigma_{H,i}$	6.73(1)	19.04(1)	26.25(2)	14.96(1)	4.16(1)
$\frac{\sigma_{H,i}}{\sigma_H}$	0.852	0.938	1.005	1.018	0.983

Table 5: Cross sections for $gg \rightarrow H \rightarrow W^+(\rightarrow \nu_e e^+)W^-(\rightarrow \mu^- \bar{\nu}_\mu)$ in femtobarns at $\sqrt{s} = 7$ TeV with no cuts applied, computed at leading order and either excluding (σ_H) or including ($\sigma_{H,i}$) the effect of interference with the gluon-initiated background process.

Numerical values of these cross section are shown in Table 5 for a selection of benchmark Higgs masses. We observe that the relative size of the interference is strongly dependent on the Higgs mass and that the interference changes sign at the $m_H = 2m_W$ threshold. For $m_H > 2m_W$ there are two further changes of sign, with a minimum at $m_H = 2m_t$. For very large Higgs masses the interference becomes large and positive. For reference we have also plotted in Fig. 6 the contribution to the interference from the first two generations of quarks only (i.e. setting $\mathcal{A}_{\text{massive}} = 0$ in the definitions of Eq. (4.1)). The difference between

the two and three generation results is striking. Except for values of $m_H \lesssim 200$ GeV, in general either the sign or the magnitude of the two-generation interference is changed in the three-generation result. This is a result of features in the three-generation result around $m_H = 2m_t$, as is expected from the thresholds of the integral functions. We conclude that, despite being a negligible factor in total rates, it is imperative to include the massive loop contribution in calculations of interference effects. For the lightest Higgs mass considered here, ($m_H = 120$ GeV) the prediction for the Higgs cross section including interference effects ($\sigma_{H,i}$) is 10 – 15% lower than would be anticipated with the usual approach (σ_H). Since a $\mathcal{O}(10\%)$ correction competes with the theoretical uncertainty of the NNLO cross section these pieces should be included in the prediction for a light Higgs cross section at the LHC. For $m_H > 400$ GeV the interference becomes large and constructive, although one should take care in interpreting the results in this region since for these values of m_H the Higgs width becomes very large (c.f. Table 2). For instance, including an \hat{s} -dependent width for the Higgs boson would change the details of the results at large m_H .

A detailed examination of the interference can be performed by separating the Breit-Wigner form of the Higgs boson propagator into its real and imaginary parts. Thus the result for the interference can be written as,

$$\delta\sigma_i = \frac{(\hat{s} - m_H^2)}{(\hat{s} - m_H^2)^2 + m_H^2 \Gamma_H^2} \Re \left\{ 2\tilde{\mathcal{A}}_{\text{Higgs}} \mathcal{A}_{\text{box}}^* \right\} + \frac{m_H \Gamma_H}{(\hat{s} - m_H^2)^2 + m_H^2 \Gamma_H^2} \Im \left\{ 2\tilde{\mathcal{A}}_{\text{Higgs}} \mathcal{A}_{\text{box}}^* \right\}, \quad (4.2)$$

where $\tilde{\mathcal{A}}_{\text{Higgs}} = (\hat{s} - m_H^2 + im_H \Gamma_H) \mathcal{A}_{\text{Higgs}}$. Although in the above equation the dependence of $\tilde{\mathcal{A}}_{\text{Higgs}}$ and \mathcal{A}_{box} on the kinematic variables has been suppressed, both $\tilde{\mathcal{A}}_{\text{Higgs}}$ and \mathcal{A}_{box} contain thresholds and other kinematic structures. The results for the two terms in Eq. (4.2) are shown in Fig. 7 as a function of the invariant mass of the four final state leptons, $m_{4\ell}$. Although $m_{4\ell}$ is not an experimentally-measurable quantity, it is particularly important since it is equal to \hat{s} , the partonic centre of mass energy, at this order. We show results for Higgs masses of 120 and 600 GeV. For $m_H = 120$ GeV the width of the Higgs boson is very small (3.6 MeV) and hence the contribution of the imaginary part is negligible. The kinematic structure in the real part means that the \hat{s} -dependence extracted in Eq. (4.2) is not a faithful representation of the full dependence. Consequently, the dominant contribution to the interference comes from the real part of the Breit-Wigner as can be seen in Fig. 7. For $m_H = 600$ GeV the imaginary part contributes about a third of the net interference. Although some cancellation between the region $\hat{s} < m_H^2$ and $\hat{s} > m_H^2$ is apparent, the net contribution is positive. For reference, in Fig. 7 we also show the contribution of the real part computed using two massless generations of quarks, which exhibits less kinematic structure.

In Fig. 8 we present the distribution of $m_{4\ell}$, combining the Higgs signal (σ_H or $\sigma_{H,i}$) with the background (σ_B), for two different Higgs masses. We have chosen to compare the quantities $d(\sigma_H + \sigma_B)/dm_{4\ell}$ and $d(\sigma_{H,i} + \sigma_B)/dm_{4\ell}$ so that the distribution is positive throughout. In Refs. [13, 14] it was shown that, for the case of ZZ production, unitarity requires destructive interference between the Higgs and non-resonant contributions in the limit of large \hat{s} . From our study of the interference as a function of m_H , depicted in Fig. 6,

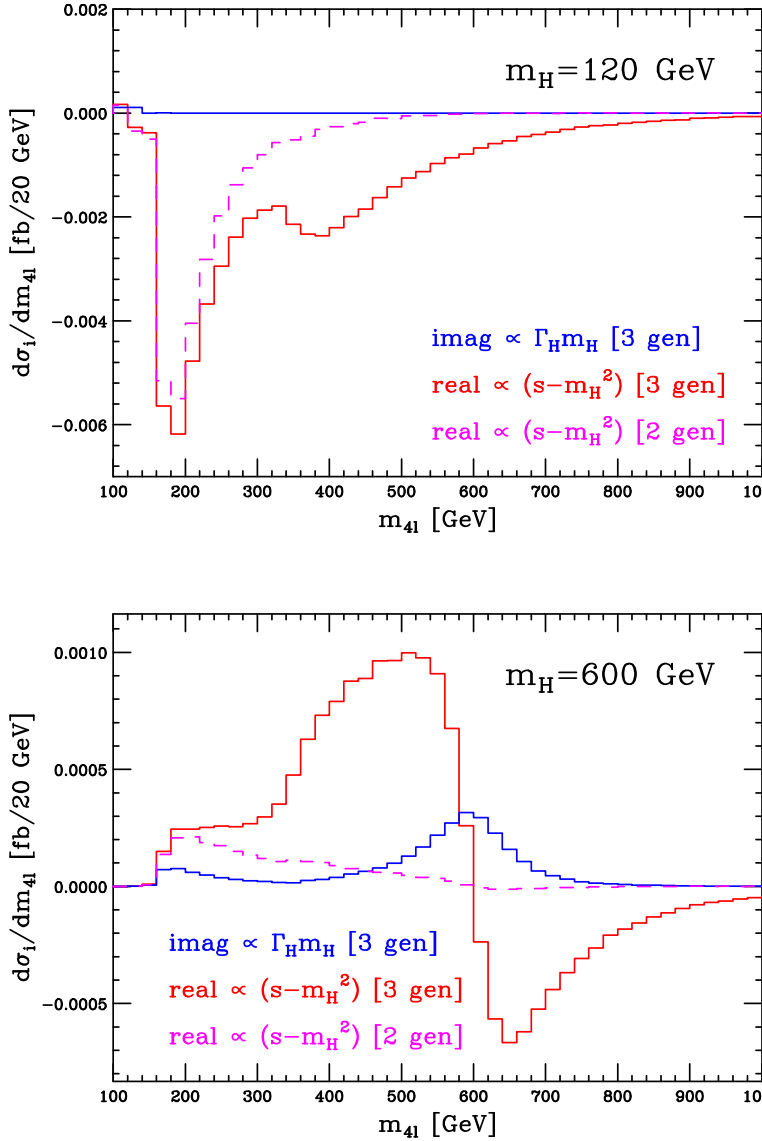


Figure 7: Contributions to the interference coming from the real (red) and imaginary (blue) part of the Higgs Breit-Wigner propagator, as defined in Eq. (4.2), for two values of the Higgs mass. The real part of the interference with two generations of massless quarks is shown by the dashed magenta line.

one might worry that the constructive interference at large m_H violates the \hat{s} requirement. However, Fig. 8 illustrates that this is not the case. Although there is a net constructive interference for $m_H = 600$ GeV, this is due to the large enhancement of the cross section in the region $\hat{s} < m_H$. In the limit of large \hat{s} we observe that the interference is large and destructive, in complete agreement with the findings of refs. [13, 14]. For a much lighter Higgs boson, for instance $m_H = 120$ GeV, there is no significant increase of the cross section in the region $\hat{s} < m_H$ and the net destructive contribution simply results from the destructive interference in the tail.

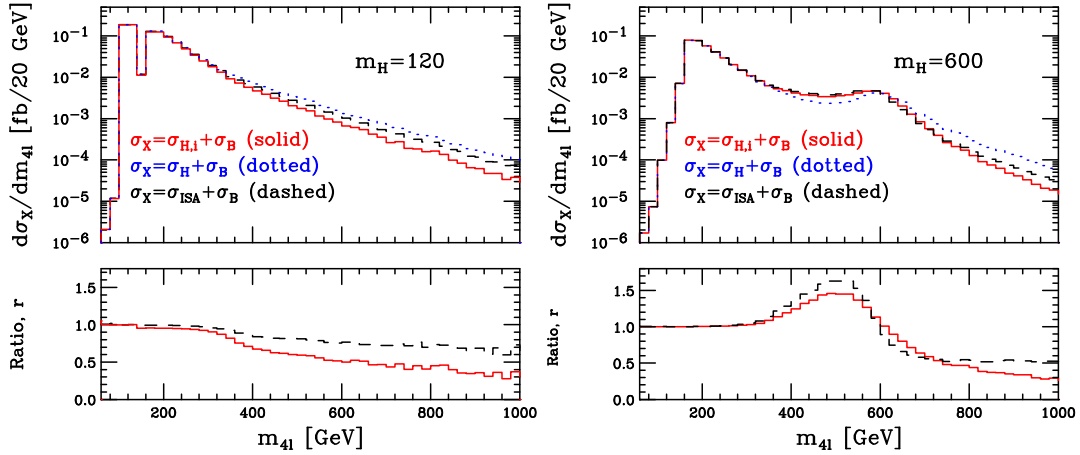


Figure 8: The upper panels present results for the invariant mass of the four final state leptons using $\sigma_H + \sigma_B$ (blue dotted) and $\sigma_{H,i} + \sigma_B$ (red solid) for two different Higgs masses (left $m_H = 120$, right $m_H = 600$). In addition we plot the distribution with no interference terms but using the rescaled Higgs propagator, $\sigma_{ISA} + \sigma_B$ [10, 37] (black dashed). In the lower panels we present the ratio $r = [d(\sigma_{H,i} + \sigma_B)/dm_{4\ell}] / [d(\sigma_H + \sigma_B)/dm_{4\ell}]$ (red solid) and $r = [d(\sigma_{ISA} + \sigma_B)/dm_{4\ell}] / [d(\sigma_H + \sigma_B)/dm_{4\ell}]$ (dashed) .

A method recently employed in ref. [10] to attempt to approximate the interference effects is based on the “improved s-channel approximation” (ISA) of ref. [37]. The prescription for unitarizing the amplitude is obtained by modifying the Higgs boson propagator,

$$\frac{i\hat{s}}{\hat{s} - m_H^2} \rightarrow \frac{im_H^2}{\hat{s} - m_H^2 + i\Gamma_H(m_H)\frac{\hat{s}}{m_H}}. \quad (4.3)$$

In order to test this approximation, in Fig. 8 we also show the $m_{4\ell}$ distribution calculated using this approach, denoted σ_{ISA} . We observe that, as expected, the modified propagator decreases the cross section in the limit of large $m_{4\ell}$ (\hat{s}). We note that although the ISA approach has some of the features of the interference that we observe, there are significant differences in shape between the two approaches across the entire $m_{4\ell}$ range.

4.2 Interference with search cuts

We now investigate the effect of the interference with more realistic search cuts mimicking those used by the CMS and ATLAS collaborations. To provide results for the CMS collaboration we use the cuts that were employed in the search for the Higgs boson in the 2010 data set [1]. Basic acceptance cuts are always applied to the missing transverse energy (E_t) and lepton rapidities,

$$E_t > 20 \text{ GeV}, \quad |\eta_\ell| < 2.5, \quad (4.4)$$

and then a number of further cuts are optimised for different values of the Higgs mass. In particular, cuts on the transverse momenta of the two leptons ($p_T^{\ell_{max}}, p_T^{\ell_{min}}$), the invariant

m_H [GeV]	p_T^h [GeV]	p_T^s [GeV]	m_{cut} [GeV]	$\Delta\phi_{\text{cut}}$
130	25	20	45	60°
160	30	25	50	60°
200	40	25	90	100°

Table 6: Kinematic cuts used by CMS (taken from Ref. [1]) for a selection of potential Higgs masses. Cuts represent the lower limits on the lepton p_T for the hardest and softest leptons, the upper limit on the invariant mass of the leptons $m_{\ell\ell}$ and the maximum azimuthal angular separation between the leptons, $\Delta\phi_{\ell\ell}$ (c.f. Eq. (4.5)).

mass of the lepton pair ($m_{\ell\ell}$) and the azimuthal angle between the leptons ($\Delta\phi_{\ell\ell}$) are all dependent on the value of m_H that is assumed in the search. These cuts take the form,

$$p_T^{\ell_{\text{max}}} > p_T^h, \quad p_T^{\ell_{\text{min}}} > p_T^s, \quad m_{\ell\ell} < m_{\text{cut}}, \quad \Delta\phi_{\ell\ell} < \Delta\phi_{\text{cut}}, \quad (4.5)$$

where the cut thresholds for some benchmark values of m_H are presented in Table 6.

The cuts adopted by the ATLAS collaboration [3] are as follows. The set of basic acceptance cuts is,

$$p_T^{\ell_{\text{max}}} > 20 \text{ GeV}, \quad p_T^{\ell_{\text{min}}} > 15 \text{ GeV}, \quad \cancel{E}_T > 30 \text{ GeV}, \quad |\eta_\ell| < 2.5, \quad (4.6)$$

and a further two cuts are applied that depend only on whether or not the putative Higgs boson is lighter than 170 GeV,

$$m_{\ell\ell} < 50 \text{ (60) GeV}, \quad \Delta\phi_{\ell\ell} < 1.3 \text{ (1.8)}, \quad (4.7)$$

(numbers in parentheses indicate the values for $m_H > 170$ GeV). In addition, the transverse mass M_T is constrained to be in the region $0.75 m_H < M_T < m_H$, where M_T is defined as,

$$M_T = \sqrt{(E_T^{\ell\ell} + E_T^{\text{miss}})^2 - (\mathbf{p}_T^{\ell\ell} + \mathbf{p}_T^{\text{miss}})^2} \quad (4.8)$$

and $E_T^{\ell\ell} = \sqrt{(\mathbf{p}_T^{\ell\ell})^2 + m_{\ell\ell}^2}$.

Our results for the cross sections with each set of cuts, with and without the interference terms, are depicted in Fig. 9 and tabulated for three values of m_H in Table 7. For this study we have focused primarily on lighter Higgs bosons, where the $H \rightarrow WW$ search channel is most relevant, and have considered three different choices of scale, $(m_H/2, m_H, 2m_H)$ when evaluating our predictions. At first sight the results appear qualitatively similar. As might be expected, the relative effect of the interference is insensitive to the choice of scale and grows with m_H , as already observed for the case of no cuts in Fig. 6. Although the ratio of $\sigma_{H,i}$ to σ_H is similar for both sets of cuts above 160 GeV, there are major differences in the overall impact of the interference terms in the low mass region, $m_H \lesssim 140$ GeV. In this region one finds that, using the CMS cuts, the interference is destructive and leads to a reduction of around 10% in the Higgs signal cross section. On the other hand, the result of the interference terms after the application of the ATLAS cuts is an order of magnitude smaller, around 1%.

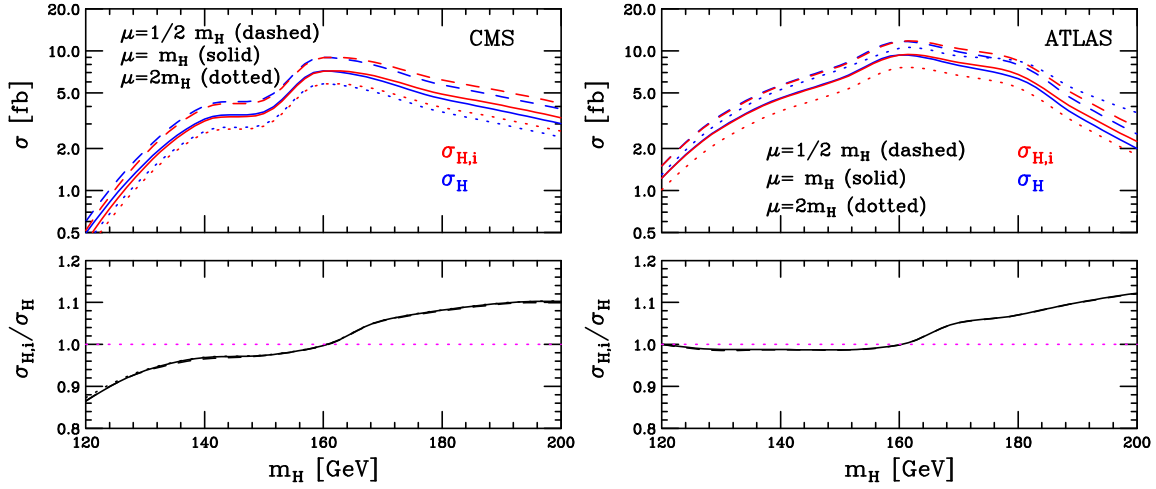


Figure 9: Cross sections for $gg \rightarrow H \rightarrow W^+(\rightarrow \nu_e e^+)W^-(\rightarrow \mu^- \bar{\nu}_\mu)$ in femtobarns with and without interference effects using the CMS (left) and ATLAS (right) Higgs search cuts [1, 3]. The red curves include the effects of the interference whilst the blue curves do not. We evaluate the cross section at three different scales $m_H/2$ (dashed), m_H (solid) and $2m_H$ (dotted). The lower panel shows the ratio between the cross sections with and without the interference, evaluated using each of the three scale choices.

Experiment	CMS			ATLAS		
M_H [GeV]	130	160	200	130	160	200
σ_H	1.58	7.18	3.02	2.82	9.35	2.00
$\sigma_{H,i}$	1.48	7.16	3.33	2.79	9.34	2.24
$\frac{\sigma_{H,i}}{\sigma_H}$	0.94	1.00	1.10	0.99	1.00	1.12

Table 7: Cross sections for $gg \rightarrow H \rightarrow W^+(\rightarrow \nu_e e^+)W^-(\rightarrow \mu^- \bar{\nu}_\mu)$ in femtobarns at $\sqrt{s} = 7$ TeV with typical experimental Higgs search cuts applied (see Ref. [1, 3]), computed at leading order and either excluding (σ_H) or including ($\sigma_{H,i}$) the effect of interference with the gluon-initiated background process.

The large destructive interference effects under the CMS cuts are not surprising since similar results are found when no cuts are applied, c.f. Fig. 6. We now investigate the ATLAS cuts in order to understand the origin of these destructive effects in the low mass region and why they are absent for this choice of cuts. The only major difference between the ATLAS and the CMS (or no) cuts is the application of the cut on the transverse mass of the system. We therefore present the M_T distribution for $m_H = 120$ GeV, with no cuts applied, in Fig. 10. It is clear that the M_T distribution has a kinematic edge at $M_T = m_H$ since, if the Higgs were always produced on-shell, the transverse mass M_T would be zero at this order in the region $M_T > m_H$. However, small finite width effects ensure that this distribution has a small (but non-zero) tail. This argument holds for the resonant Higgs contributions to the amplitudes, but the non-resonant box diagrams have no such kinematic edge and instead can be relatively large in the $M_T > m_H$ region. As a result the interference

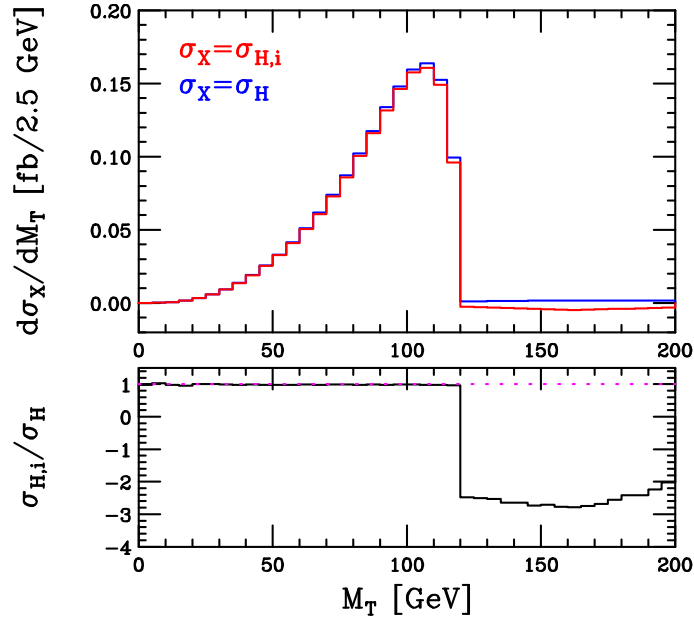


Figure 10: The M_T distribution for a Higgs mass of 120 GeV with no cuts applied (upper panel). The lower (red) histogram is calculated including the effects of the interference term whilst the upper (blue) curve is obtained using the Higgs amplitude only. The ratio of the red and blue curves is shown in the lower panel.

terms in this region have a large effect. In the region $M_T > m_H$ we see that the prediction for what appears to be a cross section is actually negative. However $\sigma_{H,i}$ is not a true physical cross section, it is merely the change in the cross section induced by the presence of the Higgs boson in the calculation of the relevant amplitudes. To obtain a physical cross section, one would have to add the contribution from the background squared, σ_B . This contribution is large and positive and as a result the physical cross section remains positive. The destructive interference at large M_T is of course just a reflection of the expected destructive interference at large \hat{s} already discussed in Section 4.1 and illustrated in Figs. 7 and 8.

From this figure we can therefore conclude that the M_T cut employed by ATLAS naturally removes the region of phase space in which the interference is destructive and, as a result $\sigma_{H,i}/\sigma_H \sim 1$ under the ATLAS cuts. It is also important, however, to quantify the effect of the interference on other kinematic distributions. One important example is the azimuthal angle between the leptons ($\Delta\phi_{\ell\ell}$) which is used in the search cuts of Eqs. (4.5,4.7). Since the Higgs signal peaks at low $\Delta\phi_{\ell\ell}$ and the background peaks in the region close to $\Delta\phi_{\ell\ell} = \pi$, this variable is a strong discriminant between signal-like and background-like events. Our predictions for this distribution, using $m_H = 120$ GeV, are shown in Fig. 11. We observe that with no cuts applied there is a non-trivial shape change in $\Delta\phi_{\ell\ell}$. However, after the application of the cuts in Eqs. (4.6,4.7) and the M_T constraint, the shape change is negligible. This suggests that it is safe to use the ratio $\sigma_{H,i}/\sigma_H$ as an overall re-weighting constant under these cuts.

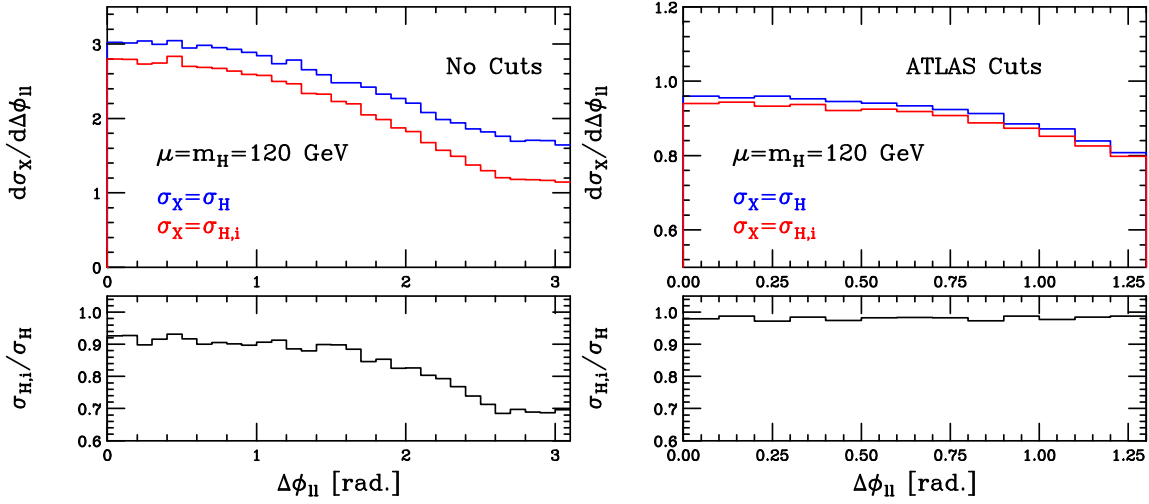


Figure 11: The $\Delta\phi_{\ell\ell}$ distribution for a Higgs mass of 120 GeV, both with no cuts applied (left) and using the ATLAS cuts (right). The lower (red) histograms are calculated including the effects of the interference ($\sigma_{H,i}$) while the upper (blue) curves are obtained using the Higgs amplitudes (σ_H) only. In the lower panel we plot the ratio of the two curves.

To summarise, we would advocate the use of an upper limit on M_T in Higgs searches in the WW channel, for instance as currently used by the ATLAS collaboration. In addition to serving as a cut that reduces Standard Model backgrounds, it also reduces the destructive interference between the SM and Higgs amplitudes by around 10%, thereby increasing the expected Higgs signal.

5. Higgs $\rightarrow WW$ interference effects at the Tevatron

The CDF and D0 experiments at the Tevatron also use the WW channel to search for the Higgs boson in the mass range 120–200 GeV [2]. Since we are discussing gluon-gluon initial states the difference between the $p\bar{p}$ and pp colliders is immaterial and for this analysis the Tevatron and the LHC differ only in their centre of mass energies. The Higgs cross section at the Tevatron has been studied in great detail [4–10], resulting in a theoretical uncertainty that is taken to be $\mathcal{O}(10\%)$ [2]. Since the interference effects that we have studied so far at the LHC contribute at precisely this level, in this section we perform a more detailed study in order to quantify the effects in the Tevatron search region.

We examine the effect of the interference both with no cuts and with typical search cuts used in the experimental analyses. Since the cuts used by CDF and D0 do not differ significantly, we choose here to focus on the set of cuts employed in recent CDF analyses [2, 38]. Specifically, we require,

$$\begin{aligned} p_T^{\ell_{max}} &> 20 \text{ GeV}, & |\eta^{\ell_{max}}| &< 0.8, \\ p_T^{\ell_{min}} &> 10 \text{ GeV}, & |\eta^{\ell_{min}}| &< 1.1, & m_{\ell\ell} &> 16 \text{ GeV}. \end{aligned} \quad (5.1)$$

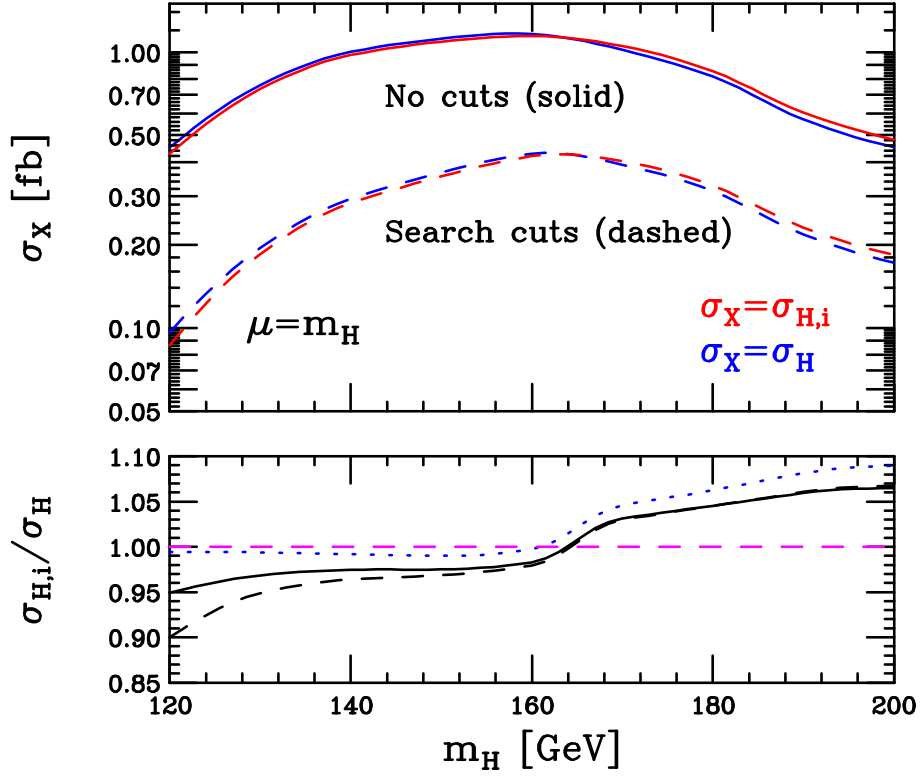


Figure 12: Cross sections for $gg \rightarrow H \rightarrow W^+(\rightarrow \nu_e e^+)W^-(\rightarrow \mu^- \bar{\nu}_\mu)$ in femtobarns at the Tevatron, with and without interference effects. The cross sections are computed by applying the Higgs search cuts (lower curves) or not (upper curves). The red curves include the effects of the interference whilst the blue curves do not. The lower panel shows the ratio $\sigma_{H,i}/\sigma_H$ for no cuts (solid), search cuts (dashed) and search cuts with an additional constraint $M_T < m_H$ (dotted).

In addition the missing transverse momentum is constrained using the $\cancel{E}_t^{\text{spec}}$ variable defined by [38],

$$\cancel{E}_t^{\text{spec}} = \cancel{E}_t \sin \left[\min \left(\Delta\phi, \frac{\pi}{2} \right) \right]. \quad (5.2)$$

$\Delta\phi$ is the distance between the \cancel{E}_t vector and the nearest lepton or jet. We require that $\cancel{E}_t^{\text{spec}} > 25$ GeV.

Our results both with and without this set of cuts are presented in Fig. 12. We observe that with no cuts the interference has the same structure as at the LHC. For $m_H < 2m_W$ the effect is destructive and of the order 5% for $m_H < 130$ GeV. Around $m_H \sim 2m_W$ the effects are very small whilst for higher m_H the effect is around 5% and constructive. We also observe that applying the search cuts increases the magnitude of the destructive interference in the low mass region. This effect, at the level of 10% for $m_H = 120$ GeV, is as large as the theoretical uncertainty estimated from the NNLO cross section. The effect of the interference on current Tevatron analyses should therefore be taken into account.

In the previous section we observed that a cut on the transverse mass M_T effectively eliminated the region of destructive interference. We have therefore recalculated the quan-

ties $\sigma_{H,i}$ and σ_H at the Tevatron, using the same CDF cuts described above but with an additional requirement that $M_T < m_H$. Under these cuts we indeed find that the impact of the interference is reduced considerably, from $\mathcal{O}(10\%)$ to $\mathcal{O}(1\%)$ just as at the LHC. The results for the interference with the additional M_T cut are illustrated by the dotted blue curve in Fig. 12.

6. Combining the interference with NNLO predictions

In this paper we have computed the interference between Higgs and continuum contributions at leading order, i.e. between the production of a Higgs boson via a top (or bottom) quark triangle and a $gg \rightarrow WW$ box diagram. To calculate the interference at the next order one would need the NLO corrections to the Higgs process (which are known) and the NLO corrections to the gluon-gluon process (which are not). The NNLO result for the Higgs process has of course been known for some time [4–10], with large (factor of two) corrections to the LO cross section.

A natural question arises as to how our results for the interference should be combined with the NNLO Higgs production cross section. One could simply modify the NNLO cross section by adding the LO interference terms, i.e. by defining,

$$\sigma_{H,i}^{NNLO} = \sigma_H^{NNLO} + (\sigma_{H,i}^{LO} - \sigma_H^{LO}). \quad (6.1)$$

Since σ_H^{NNLO} is much larger than $\sigma_{H,i}^{LO}$ one would expect that using Eq. (6.1) to estimate the effect of the interference would reduce the results in this paper by approximately a factor of two.

However, treating the interference as an absolute correction to the NNLO cross section neglects the effect of all higher orders on the interference. Although the Higgs process receives large corrections at NLO and NNLO, the corresponding corrections to the gluon-gluon box diagram processes are unknown. Since we are not able to quantify these corrections a more conservative approach (particularly in the low-mass region where interference effects are large) would be to re-weight the NNLO cross section by the relative effect of the interference at LO, i.e. define,

$$\sigma_{H,i}^{NNLO} = \sigma_H^{NNLO} \left(\frac{\sigma_{H,i}^{LO}}{\sigma_H^{LO}} \right). \quad (6.2)$$

It is this approach that we recommend in the region where the interference is destructive.

7. Conclusions

In this paper we studied the production of WW pairs through gluon fusion in the Standard Model. This process proceeds at loop-level through a closed fermion loop. In a previous paper [24] we presented analytic results for massless fermions, which correspond to the first two generations circulating in the loop. We extended these results to include contributions from the third generation keeping the full dependence on the top mass m_t . These formulae have been implemented into MCFMv6.1 which will soon be publicly available. The process

$gg \rightarrow WW \rightarrow \nu \ell^+ \ell'^- \bar{\nu}'$ keeping the full top (and bottom) mass dependence was previously calculated in ref. [12] using a semi-numerical approach.

The amplitude for $gg \rightarrow WW$ with non-zero m_t can be written in the usual one-loop expansion in terms of scalar integrals. We found that the rational terms and all but two bubble coefficients were identical to the massless result. Further, the remaining two bubble coefficients were found to sum to the equivalent $m_t = 0$ coefficient. As a result we only needed to calculate one bubble coefficient. We used generalised unitarity techniques to calculate the box and triangle coefficients, which differ from the massless results.

One of the most important phenomenological applications of these results is the effect on the Higgs/SM continuum interference. We illustrated that in general there are big deviations between the 2 and 3 generation calculations of this interference. It is crucial to quantify the impact of the interference as a function of the putative Higgs mass and under a variety of cuts, since in general these terms can contribute changes in rates comparable to the theoretical uncertainty associated with a NNLO prediction for the cross section. We found that in general the interference is largest far away from the $2m_W$ threshold. For large m_H ($> 2m_t$) the interference is constructive and for low ($m_H < 140$ GeV) masses it is destructive. In the region $120 < m_H < 130$ GeV the destructive interference reduces the total cross section by around 10–15%. This large interference originates from non-resonant contributions above m_H .

We illustrated that the interference is sensitive to the experimental cuts under consideration and that cuts used in the 2010 ATLAS analysis [3] dramatically reduce the large destructive interference for small m_H . We showed that this is a result of the M_T cut that is employed, in particular the upper bound that effectively removes the non-resonant contribution to the interference. After applying the cut $M_T < m_H$, the interference is reduced from $\mathcal{O}(10\%)$ to $\mathcal{O}(1\%)$. Therefore we would advocate the use of the cut $M_T < m_H$ for all experiments at hadron colliders since this enhances the signal by removing the region in which the destructive interference dominates.

The total $gg \rightarrow H$ cross section is known to NNLO [4–10] accuracy and the K -factor from going from LO to NNLO is large. Therefore, if the interference is treated as an absolute correction to the NNLO cross section its impact is reduced by an approximate factor of two. However, the interference is present at every order in perturbation theory and as such a more conservative approach would be to re-weight the NNLO cross section by the relative effect of the interference at LO. The size of the interference means that this is particularly important when setting Higgs mass limits using this channel for $m_H \lesssim 140$ GeV.

Acknowledgements

We thank Joey Huston, Bruce Mellado, Kirill Melnikov and Frank Petriello for useful discussions. Fermilab is operated by Fermi Research Alliance, LLC under Contract No. DE-AC02-07CH11359 with the United States Department of Energy.

References

- [1] **CMS** Collaboration, S. Chatrchyan *et. al.*, *Measurement of WW Production and Search for the Higgs Boson in pp Collisions at $\sqrt{s} = 7$ TeV*, *Phys. Lett.* **B699** (2011) 25–47 [[1102.5429](#)].
- [2] **CDF and D0** Collaboration, T. Aaltonen *et. al.*, *Combined CDF and D0 Upper Limits on Standard Model Higgs Boson Production with up to 8.2 fb⁻¹ of Data*, [1103.3233](#).
- [3] **ATLAS** Collaboration, G. Aad *et. al.*, *Limits on the production of the Standard Model Higgs Boson in pp collisions at $\sqrt{s} = 7$ TeV with the ATLAS detector*, [1106.2748](#).
- [4] C. Anastasiou and K. Melnikov, *Higgs boson production at hadron colliders in NNLO QCD*, *Nucl. Phys.* **B646** (2002) 220–256 [[hep-ph/0207004](#)].
- [5] V. Ravindran, J. Smith and W. L. van Neerven, *NNLO corrections to the total cross section for Higgs boson production in hadron hadron collisions*, *Nucl. Phys.* **B665** (2003) 325–366 [[hep-ph/0302135](#)].
- [6] C. Anastasiou, K. Melnikov and F. Petriello, *Higgs boson production at hadron colliders: Differential cross sections through next-to-next-to-leading order*, *Phys. Rev. Lett.* **93** (2004) 262002 [[hep-ph/0409088](#)].
- [7] C. Anastasiou, G. Dissertori and F. Stockli, *NNLO QCD predictions for the $H \rightarrow WW \rightarrow l l \nu \nu$ signal at the LHC*, *JHEP* **09** (2007) 018 [[0707.2373](#)].
- [8] S. Catani and M. Grazzini, *An NNLO subtraction formalism in hadron collisions and its application to Higgs boson production at the LHC*, *Phys. Rev. Lett.* **98** (2007) 222002 [[hep-ph/0703012](#)].
- [9] M. Grazzini, *NNLO predictions for the Higgs boson signal in the $H \rightarrow WW \rightarrow l \nu l \nu$ and $H \rightarrow ZZ \rightarrow 4l$ decay channels*, *JHEP* **02** (2008) 043 [[0801.3232](#)].
- [10] C. Anastasiou, S. Buehler, F. Herzog and A. Lazopoulos, *Total cross-section for Higgs boson hadroproduction with anomalous Standard Model interactions*, [1107.0683](#).
- [11] **LHC Higgs Cross Section Working Group** Collaboration, S. Dittmaier *et. al.*, *Handbook of LHC Higgs Cross Sections: 1. Inclusive Observables*, [1101.0593](#).
- [12] T. Binoth, M. Ciccolini, N. Kauer and M. Kramer, *Gluon-induced W -boson pair production at the LHC*, *JHEP* **12** (2006) 046 [[hep-ph/0611170](#)].
- [13] E. Glover and J. van der Bij, *Vector boson pair production via gluon fusion*, *Phys.Lett.* **B219** (1989) 488.

- [14] E. W. N. Glover and J. J. van der Bij, *Z boson pair production via gluon fusion*, *Nucl. Phys.* **B321** (1989) 561.
- [15] L. J. Dixon and M. Siu, *Resonance continuum interference in the diphoton Higgs signal at the LHC*, *Phys.Rev.Lett.* **90** (2003) 252001 [[hep-ph/0302233](#)].
- [16] L. J. Dixon and Y. Sofianatos, *Resonance-Continuum Interference in Light Higgs Boson Production at a Photon Collider*, *Phys.Rev.* **D79** (2009) 033002 [[0812.3712](#)].
- [17] R. W. Brown and K. O. Mikaelian, *$W^+ W^-$ and $Z^0 Z^0$ Pair Production in $e^+ e^-$, $p p$, p anti- p Colliding Beams*, *Phys. Rev.* **D19** (1979) 922.
- [18] J. Ohnemus, *An Order α_s calculation of hadronic $W^- W^+$ production*, *Phys. Rev.* **D44** (1991) 1403–1414.
- [19] S. Frixione, *A Next-to-leading order calculation of the cross-section for the production of $W^+ W^-$ pairs in hadronic collisions*, *Nucl.Phys.* **B410** (1993) 280–324.
- [20] J. Ohnemus, *Hadronic ZZ , $W^- W^+$, and $W^\pm Z$ production with QCD corrections and leptonic decays*, *Phys. Rev.* **D50** (1994) 1931–1945 [[hep-ph/9403331](#)].
- [21] L. J. Dixon, Z. Kunszt and A. Signer, *Helicity amplitudes for $O(\alpha_s)$ production of $W^+ W^-$, $W^\pm Z$, ZZ , $W^\pm \gamma$, or $Z \gamma$ pairs at hadron colliders*, *Nucl. Phys.* **B531** (1998) 3–23 [[hep-ph/9803250](#)].
- [22] J. M. Campbell and R. K. Ellis, *An update on vector boson pair production at hadron colliders*, *Phys. Rev.* **D60** (1999) 113006 [[hep-ph/9905386](#)].
- [23] L. J. Dixon, Z. Kunszt and A. Signer, *Vector boson pair production in hadronic collisions at order $\alpha(s)$: Lepton correlations and anomalous couplings*, *Phys. Rev.* **D60** (1999) 114037 [[hep-ph/9907305](#)].
- [24] J. M. Campbell, R. K. Ellis and C. Williams, *Vector boson pair production at the LHC*, *JHEP* **07** (2011) 018 [[1105.0020](#)].
- [25] D. A. Dicus, C. Kao and W. Repko, *Gluon production of gauge bosons*, *Phys.Rev.* **D36** (1987) 1570.
- [26] T. Binoth, M. Ciccolini, N. Kauer and M. Kramer, *Gluon-induced $W W$ background to Higgs boson searches at the LHC*, *JHEP* **03** (2005) 065 [[hep-ph/0503094](#)].
- [27] Z. Bern, L. J. Dixon and D. A. Kosower, *One-loop amplitudes for $e^+ e^-$ to four partons*, *Nucl. Phys.* **B513** (1998) 3–86 [[hep-ph/9708239](#)].
- [28] J. M. Campbell, R. K. Ellis and G. Zanderighi, *Next-to-leading order predictions for $WW + 1$ jet distributions at the LHC*, *JHEP* **0712** (2007) 056 [[0710.1832](#)].
- [29] R. Ellis, W. T. Giele, Z. Kunszt and K. Melnikov, *Masses, fermions and generalized D -dimensional unitarity*, *Nucl.Phys.* **B822** (2009) 270–282 [[0806.3467](#)].

- [30] R. K. Ellis and G. Zanderighi, *Scalar one-loop integrals for QCD*, *JHEP* **0802** (2008) 002 [0712.1851].
- [31] P. Mastrolia, *Double-Cut of Scattering Amplitudes and Stokes' Theorem*, *Phys. Lett.* **B678** (2009) 246–249 [0905.2909].
- [32] R. Britto, F. Cachazo and B. Feng, *Generalized unitarity and one-loop amplitudes in $N = 4$ super-Yang-Mills*, *Nucl. Phys.* **B725** (2005) 275–305 [hep-th/0412103].
- [33] D. Forde, *Direct extraction of one-loop integral coefficients*, *Phys. Rev.* **D75** (2007) 125019 [0704.1835].
- [34] R. K. Ellis, W. J. Stirling and B. R. Webber, *QCD and collider physics*, *Camb.Monogr.Part.Phys.Nucl.Phys.Cosmol.* **8** (1996) 1–435.
- [35] A. Djouadi, J. Kalinowski and M. Spira, *HDECAY: A program for Higgs boson decays in the standard model and its supersymmetric extension*, *Comput. Phys. Commun.* **108** (1998) 56–74 [hep-ph/9704448].
- [36] A. D. Martin, W. J. Stirling, R. S. Thorne and G. Watt, *Parton distributions for the LHC*, *Eur. Phys. J.* **C63** (2009) 189–285 [0901.0002].
- [37] M. H. Seymour, *The Higgs boson line shape and perturbative unitarity*, *Phys. Lett.* **B354** (1995) 409–414 [hep-ph/9505211].
- [38] **CDF** Collaboration, *Search for $H \rightarrow WW^*$ production at CDF using 4.8fb^{-1} of data*, *CDF note 9887*.